INTERNATIONAL JOURNAL FOR NUMERICAL METHODS IN FLUIDS
Int. J. Numer. Meth. Fluids **30**: 493–508 (1999)

COMPUTATIONS OF STRONGLY SWIRLING FLOWS WITH SECOND-MOMENT CLOSURES

J.C. CHEN AND C.A. LIN*

Department of Power Mechanical Engineering, National Tsing Hua University, Hsinchu, 30043, Taiwan

SUMMARY

The present study is concerned with simulating turbulent, strongly swirling flows by eddy viscosity model and Reynolds stress transport model variants adopting linear and quadratic form of the pressure–strain models. Flows with different inlet swirl numbers, 2.25 and 0.85, were investigated. Detailed comparisons of the predicted results and measurements were presented to assess the merits of model variants. For the swirl number 2.25 case, due to the inherent capability of the Reynolds stress models to capture the strong swirl and turbulence interaction, both the linear and quadratic form of the pressure–strain models predict the flow adequately. In strong contrast, the k–ϵ model predicts an excessively diffusive flow fields. For the swirl number 0.85 case, both the k–ϵ and Reynolds stress model with linear pressure–strain process, show an excessive diffusive transport of the flow fields. The quadratic pressure–strain model, on the other hand, mimics the correct flow development with the recirculating region being correctly predicted.

KEY WORDS: flow computations; swirl; turbulence modelling

1. INTRODUCTION

From a theoretical point of view, a two-dimensional swirling flow is considerably more complicated than two-dimensional plane flows, for additional strains arise due to the azimuthal motion, requiring the solution for azimuthal momentum. Indeed, the strain field may be said to be virtually as complex as any three-dimensional flow. Swirl introduces intense azimuthal streamline curvature and hence curvature–turbulence interaction affects all six independent stress components. The effect of the elevated swirl level on the turbulence field can be exemplified by considering the flow within a circular pipe where the major mean flow component is the solid body rotation in the circumferential direction. The generations of the relevant stresses are [1],

$$P_{\overline{vw}} = (\overline{w^2} - \overline{v^2})\omega, \tag{1}$$

$$P_{\overline{ww}} - P_{\overline{vv}} = -\overline{vw}\omega, \tag{2}$$

where $\omega = W/r$ is the angular velocity. While stress levels are of course not solely determined by their productions, their values can be expected to be influential. Therefore, the above

* Correspondence to: Department of Power Mechanical Engineering, National Tsing Hua University, Hsinchu, 30043, Taiwan.

Contract/grant sponsor: National Science Council of Taiwan; Contract/grant number: NSC85-2212-E-007-023

CCC 0271–2091/99/130493–16$17.50 *Received February 1998*

relations tend to restore turbulence to isotropy and thus produce a decay of the turbulence field.

In practical applications, swirling motion is often employed as a mechanism to further promote or control mixing between the fuel spray jet and the adjacent air, and on some occasions, to stabilise the combustion zone due to the presence of the swirl-induced central recirculation region. Since the central recirculation zone induced by the decay of swirl has profound effects on flame stabilisation and mixing in combustion systems, a prior knowledge of the flow characteristics is beneficial during the design process.

Due to its importance, numerous numerical studies have been made by various researchers to study the effects of swirl in a variety of combustor geometries [2–7]. The studies demonstrate that the superiority of stress closures over the k–ϵ model in the prediction of swirling flows, though the merits of various stress model variants differ at different swirl levels and swirler type. For strongly swirling flows, for example, the superiority of the stress models [5] is reflected primarily by the lower level of shear stresses due to the proper representation of the interaction between swirl-induced curvature and stresses, as indicated earlier. Among the stress models, due to the nature of the convection and diffusion transport of stresses modelled, it was addressed [4] that the algbraic stress model (ASM) scheme is not to be used in axisymmetric swirling flows where significant stress transport processes in the overall Reynolds stress budget prevail. Instead, a Reynolds stress transport model should be adopted.

While cubic and quadratic pressure–strain models had been applied to further explore the effects of non-linear pressure–strain models on predicting free-swirling flows, the majority of the confined swirling flow predictions, however, are still limited to the linear models. The present study aims at investigating the capability of variants of Reynolds stress turbulence models, linear and quadratic pressure–strain models, on strongly swirling flows. Flows with swirl numbers 2.25 [8] and 0.85 [9] form the basis of the investigations. The higher swirler number case is designed to examine the models' response to the interaction between swirl-induced curvature and turbulence. The second case is adopted to explore the turbulence models' capability to simulate flow with the presence of extensive central recirculation region induced by the decay of the swirl intensity.

2. THE COMPUTATIONAL MODEL

2.1. The governing equations

The behaviour of the flow is in general governed by the fundamental principles of classical mechanics expressing the conservation of mass and momentum. The time-averaged equations for high Reynolds number flow, may be described by the equations (in Cartesian tensor):

$$\frac{\partial(\rho U_i)}{\partial x_i} = 0, \tag{3}$$

$$\frac{\partial(\rho U_i U_j)}{\partial x_j} = -\frac{\partial P}{\partial x_i} + \frac{\partial}{\partial x_j}\left[\mu_l\left(\frac{\partial U_i}{\partial x_j} + \frac{\partial U_j}{\partial x_i}\right) - \rho\overline{u_i u_j}\right], \tag{4}$$

where $\overline{u_i u_j}$ is the turbulent flux arising from the time averaging process. The tensorial form of the momentum equation represents the U, V and rW momentum solved.

2.2. Turbulence models

In the present application, turbulence is described either by the high Reynolds number k–ϵ eddy viscosity model [10], used here merely as a datum closure, or by one of high Reynolds number Reynolds stress closures, as detailed below, all involving six equations for the independent stresses $\overline{u_i u_j}$ and a seventh equation for the isotropic turbulence energy dissipation ϵ.

The Reynolds stress closure will be expressed in a general form, and this may be written as:

$$\frac{\partial}{\partial x_k}(\rho U_k \overline{u_i u_j}) = d_{ij} + P_{ij} + \epsilon_{ij} + \phi_{ij}, \tag{5}$$

in which d_{ij} represents diffusion and is approximated by the simplified gradient–diffusion model,

$$d_{ij} = \frac{\partial}{\partial x_k}\left[\frac{\mu_t}{\sigma_k}\frac{\partial \overline{u_i u_j}}{\partial x_k}\right]. \tag{6}$$

P_{ij} stands for the (exact) stress generation resulting from the interaction between stresses and strain,

$$P_{ij} = -\rho\overline{u_i u_k}\frac{\partial U_j}{\partial x_k} - \rho\overline{u_j u_k}\frac{\partial U_i}{\partial x_k} \tag{7}$$

and $-2/3\rho\delta_{ij}\epsilon$ models stress dissipation, ϵ_{ij}, on the assumption that this process is isotropic and may thus be characterised by the dissipation of turbulence energy ϵ.

The focal point of Reynolds stress model is the pressure–strain term ϕ_{ij}, which identifies pressure–strain interaction and consists of three model components, representing respectively, 'return to isotropy', 'isotropisation of mean strain and turbulence correlation' and 'redistributive effects arising from wall reflection of pressure fluctuations'. Variants of the pressure–strain variants were investigated.

The first stress model closure variant (IPCM) adopted here is that of Fu *et al.* [3]. This linear model is termed as the basic model by Launder and his co-workers, which may be written as:

$$\phi_{ij1} = -1.8\rho\frac{\epsilon}{k}\left[\overline{u_i u_j} - \frac{\delta_{ij}}{3}\overline{u_k u_k}\right], \tag{8}$$

$$\phi_{ij2} = -0.6\left[P_{ij} - C_{ij} - \frac{\delta_{ij}}{3}(P_{kk} - C_{kk})\right], \tag{9}$$

$$\phi_{ijw} = 0.5\rho\frac{\epsilon}{k}\left[\overline{u_k u_m}n_k n_m\delta_{ij} - \frac{3}{2}\overline{u_k u_i}n_k n_j - \frac{3}{2}\overline{u_k u_j}n_k n_i\right]f + 0.3\left[\phi_{km2}n_k n_m\delta_{ij} - \frac{3}{2}\phi_{ij2}n_k n_j - \frac{3}{2}\phi_{jk2}n_k n_i\right]f, \tag{10}$$

where

$$P_{ij} = -\rho\overline{u_i u_k}\frac{\partial U_j}{\partial x_k} - \rho\overline{u_j u_k}\frac{\partial U_i}{\partial x_k}, \qquad C_{ij} = \frac{\partial \rho U_k \overline{u_i u_j}}{\partial x_k}.$$

n_i is the wall normal unit vector in the direction i and $f = C_\mu^{0.75}k^{1.5}/(\epsilon\kappa y)$ with y being the distance to the closest wall, taken along the co-ordinate line normal to the wall.

The rate of turbulence energy dissipation ϵ, appearing in the stress equations is determined from its own transport equation, which takes the form,

$$\frac{\partial}{\partial t}(\rho\epsilon)+\frac{\partial}{\partial x_k}(\rho U_k\epsilon)=\frac{\partial}{\partial x_k}\left[\frac{\mu_t}{\sigma_\epsilon}\frac{\partial\epsilon}{\partial x_k}\right]+C_{\epsilon 1}\frac{\epsilon}{k}P_{kk}-C_{\epsilon 2}\rho\frac{\epsilon^2}{k}, \tag{11}$$

where $C_{\epsilon 1}$, $C_{\epsilon 1}$ and σ_ϵ are 1.44, 1.92 and 1.3 respectively.

Instead of the linear pressure–strain model, a second variant (SSG) proposed by Speziale *et al.* [11] employs quadratic form

$$\phi_{ij1}=-(3.4\epsilon+1.8P_k)b_{ij}+4.2\epsilon\left(b_{ik}b_{kj}-\frac{1}{3}b_{kl}b_{kl}\delta_{ij}\right), \tag{12}$$

$$\phi_{ij2}=(0.8-1.3\sqrt{b_{kl}b_{kl}})kS_{ij}+1.25k\left(b_{ik}S_{jk}+b_{jk}S_{ik}-\frac{2}{3}b_{kl}S_{kl}\delta_{ij}\right)+0.4k(b_{ik}W_{jk}+b_{jk}W_{ik}), \tag{13}$$

where

$$S_{ij}=\frac{1}{2}\left(\frac{\partial U_i}{\partial x_j}+\frac{\partial U_j}{\partial x_i}\right),\qquad W_{ij}=\frac{1}{2}\left(\frac{\partial U_i}{\partial x_j}-\frac{\partial U_j}{\partial x_i}\right),\qquad b_{ij}=\frac{\overline{u_iu_j}}{\overline{u_ku_k}}-\frac{1}{3}\delta_{ij},$$

$$P_k=-\rho\overline{u_iu_j}\frac{\partial U_i}{\partial x_j}.$$

When adopting the SSG model, the value of $C_{\epsilon 2}$ in the ϵ equation is modified to be 1.83 [11]. It should be pointed out that the SSG model does not contain a wall reflection term explicitly.

2.3. Numerical algorithm

This scheme solves discretised versions of all equations on a staggered finite volume arrangement [12]. A staggered storage is adopted not only for the velocity components but also for the shear stresses—an arrangement that aids stability by ensuring a strong numerical coupling between stresses and primary strains. The principle of mass flux continuity is imposed indirectly via the solution of pressure correction equations according to the SIMPLE [13] algorithm. The flow property values at the volume faces contained in the convective fluxes that arise from the finite volume integration process are approximated by the quadratic upstream weighted interpolation scheme QUICK [14]. The numerical meshes, of sizes 90×60 and 120×90, are non-uniform both in the x- and y-directions. Initial tests on the influences of the convection schemes revealed that the differences between the second-order QUICK and the first-order hybrid scheme were negligible small. It was also found that the two grids generate exactly the same results. Therefore, the mesh employed will be deemed to be satisfactory and further refinements of the mesh will not be beneficial.

Though the present case is a steady state solution, it was found that using a time marching process will enhance stability, especially when stress models are employed. The solution process consists of a sequential algorithm in which each of the 11 sets of equations, in linearised form, are solved separately by application of an alternate direction tri- or penta-diagonal line implicit solver. Convergence was judged by monitoring the magnitude of the absolute residual sources of mass and momentum, normalised by the respective inlet fluxes. The solution was taken as having converged when all above residuals fell below 0.01%.

3. BOUNDARY CONDITIONS

At the wall, the tangential velocity component U was assumed to vary logarithmically between the semi-viscous sublayer, at $y_v^+=11.2$, and the first computational node lying in the region

$30 < y^+ < 100$. This treatment yielded boundary conditions for the shear stresses and also permitted the volume-averaged near-wall generation rates of the tangential normal stresses to be computed over the associated near-wall finite volumes. (The generation of the wall normal intensity was assumed negligibly small) The linear variation of the turbulent length scale, $L = \kappa y / C_\mu^{3/4}$, in the log-law region, together with $\epsilon = k^{3/2}/L$, and the invariant value $\epsilon = 2\mu_l k_v / (\rho y_v^2)$ in the viscous sublayer, allowed the volume-averaged dissipation rate to be determined. This same L-variation was also used to prescribe explicitly the dissipation rate at the near-wall computational node, serving as the boundary condition for inner-field cells.

4. RESULTS AND DISCUSSIONS

4.1. Sudden expanding pipe flow

Before proceeding to the discussion of swirling flows, it is instructive to focus first on the performances of variants of turbulence models on the non-swirling sudden expanding pipe flow. The pipe expansion ratio is 1.5. The inlet velocity (U_{in}) is known to be 19.2 m s^{-1}, corresponding to a Reynolds number of 1.25×10^5 based on the inlet pipe diameter, and its inlet mean and turbulence quantities were taken from the experiment of Ahmed and Nejad [15]. Experimental data are available from $X/H = 0.38$ step heights downstream of the sudden expansion at which point the numerical simulation starts.

The capability of different models can be observed by reference to Figure 1, showing comparisons between predicted and measured axial velocity along the centreline. This indicates that the SSG model returned the best axial velocity development, though the difference among the stress models at regions $X/H < 10$ is marginal. The k–ϵ model predicted a more rapid development of axial velocity, indicating a more diffusive flow field simulated and this can be further affirmed by reference to Figure 2, which shows the predicted mean and turbulence

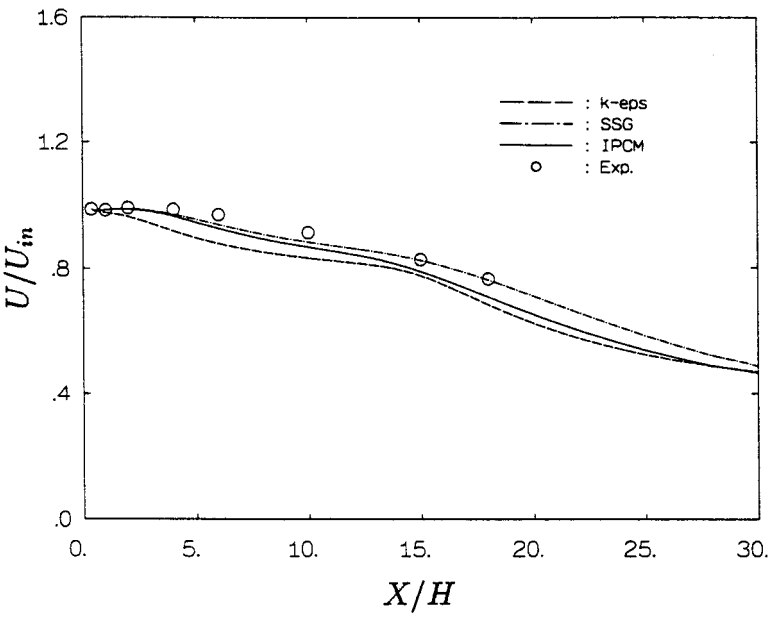

Figure 1. Centreline axial velocity—sudden expanding pipe.

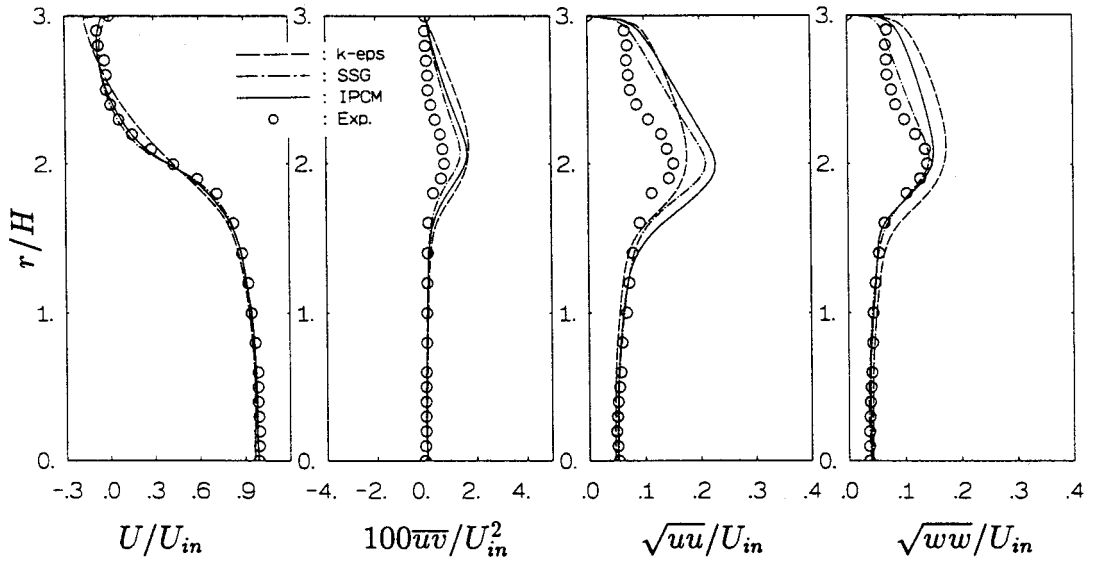

Figure 2. Comparisons of predictions and measurements at $X/H = 2$—sudden expanding pipe.

quantities at $X/H = 2$. Regarding the turbulence quantities, the SSG model also exhibited better results, a reflection of the better predicted mean flow profiles, than the rest of the models.

4.2. So et al.'s strongly swirling flow $S = 2.25$

This case is designed to examine the interaction between swirl-induced curvature and turbulence. Experimental data had been obtained by So *et al.* [8]. This consists of a pipe into which an annular swirling stream is introduced together with a non-swirling central jet. The latter is introduced to inhibit extensive reverse flow (vortex breakdown) along the centreline. The swirl number, S,

$$S = \frac{\int_0^{r_o} UWr^2 \, dr}{r_o \int_0^{r_o} U^2 r \, dr} \tag{14}$$

for this case is 2.25, where r_o is the radius of the pipe and U and W are the axial and tangential velocity respectively. According to the rule of thumb proposed by Squire [16], a subcritical state is reached when the maximum swirl velocity to the averaged streamwise velocity exceeds unity. It was found by Escudier and Keller [17] that subcritical state flow is highly sensitive to the perturbation far downstream. In the present case, the velocity ratio is well above unity and the flow is thus subcritical. Therefore, in the present computations, the exit axial velocity is prescribed from measurements to avoid the predictive uncertainties.

A subcritical state appears to reflect a strong decay in turbulent mixing, and a corresponding dominance of convective features, making the governing equations nearly hyperbolic in nature. This is confirmed from the measured axial and tangential velocity, shown in Figures 3 and 4. Stress model predictions and experimental data show the shape of the mean flow profiles to remain similar over the whole length of domain, and this implies that the mixing is weak. The

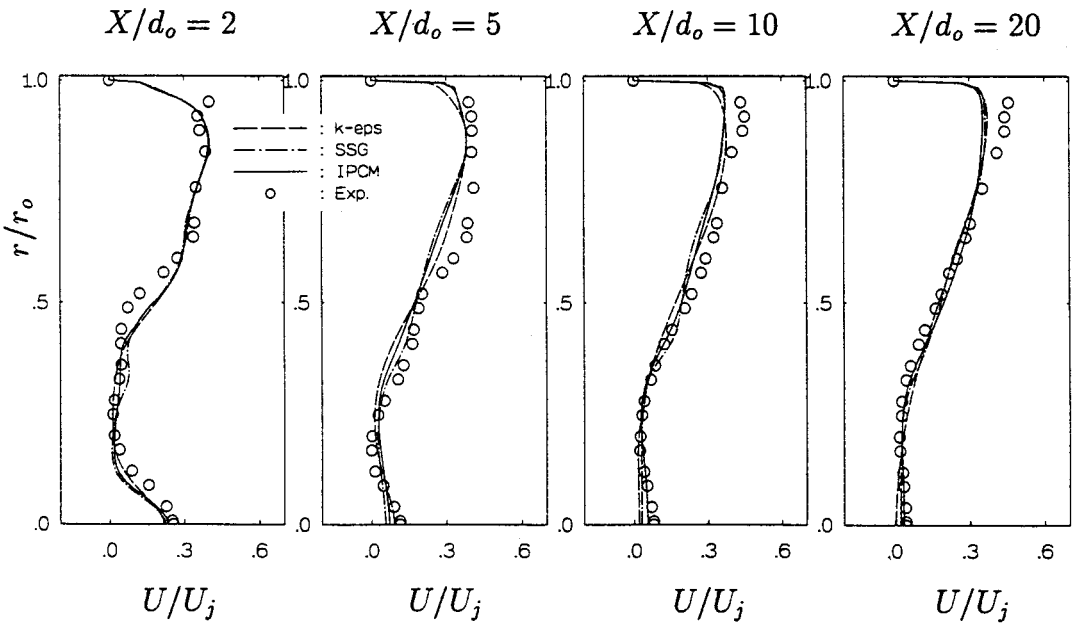

Figure 3. Axial velocity distributions—So *et al.*'s case.

k–ϵ predictions show, on the contrary, an excessively radial diffusive transport, with a faster decay of the centreline axial velocity and early return of solid body rotation of the swirling motion.

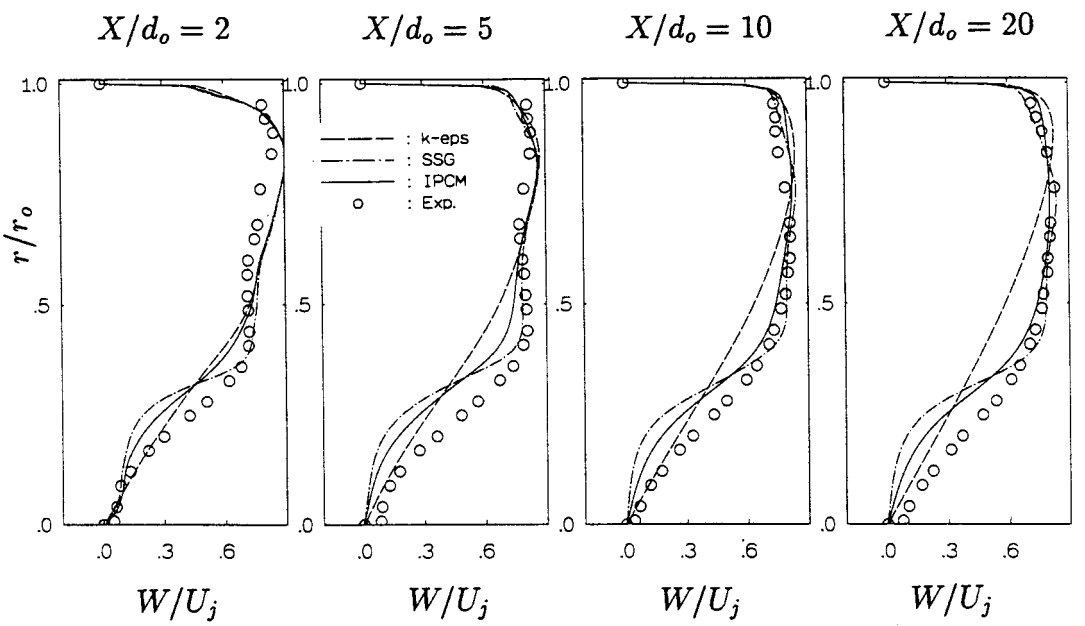

Figure 4. Tangential velocity distributions—So *et al.*'s case.

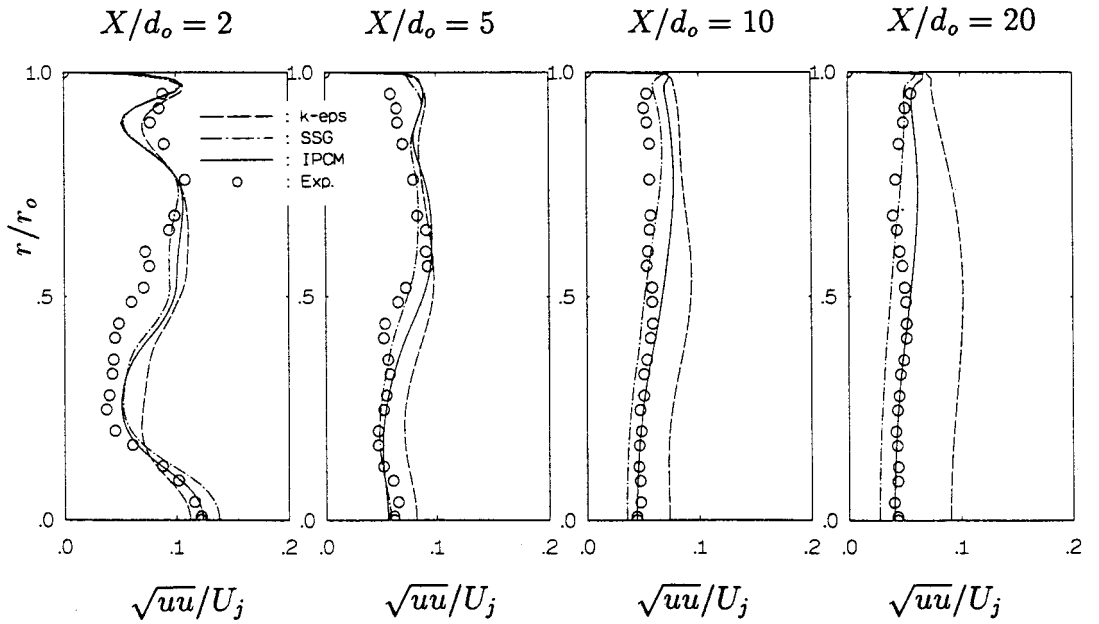

Figure 5. $\overline{uu}$ distributions—So *et al.*'s case.

Although the stress model predictions indicate a lower level of shear stresses, no measured shear stresses are available to support the simulations. Both the measurements and predictions show a nearly isotropic normal stresses. Among the predictions, the stress models return a lower level of normal stresses and agree with the measurements, shown in Figures 5 and 6. The

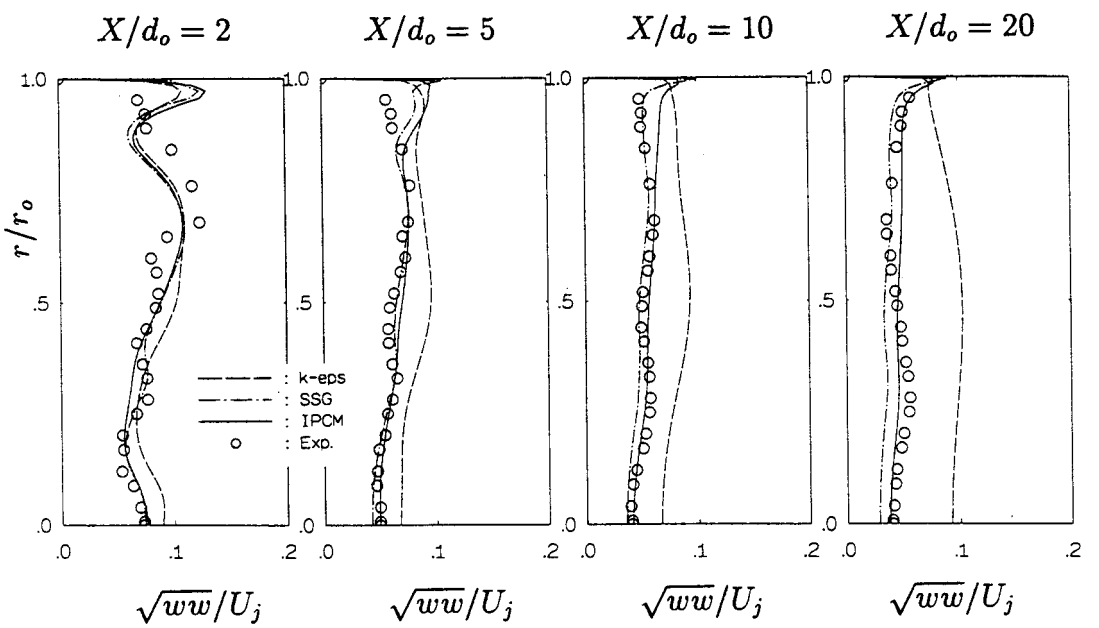

Figure 6. $\overline{ww}$ distributions—So *et al.*'s case.

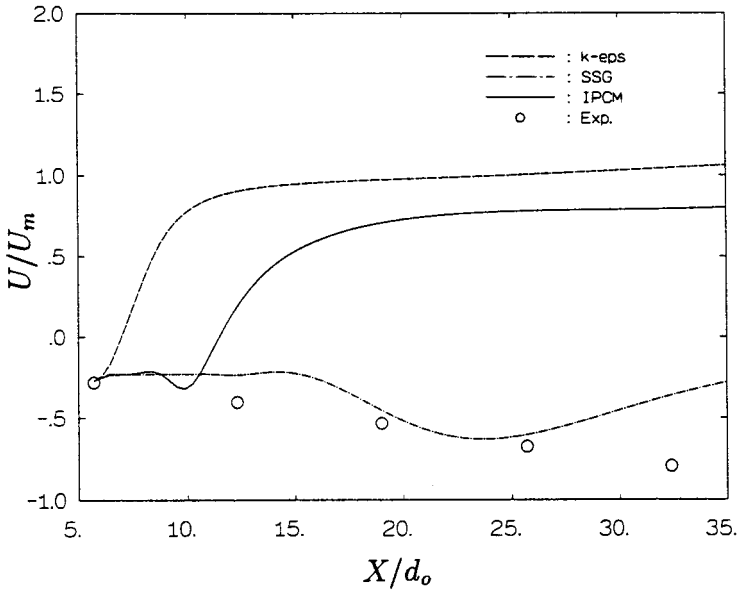

Figure 7. Centreline axial velocity distributions—Kitoh's case.

superiority of the stress models is rooted in their ability to return the depression of the shear stress levels in response to the swirl-related strain at this high level of swirling flow, and this mechanism is briefly discussed earlier. It should be noted that in the present case the difference between the linear and quadratic pressure–strain model is not significant.

4.3. Kitoh's strongly swirling flow $S = 0.85$

The present case considers swirling flow in a straight circular pipe with a free-vortex-type swirling inlet [9]. The swirl intensity, Ω,

$$\Omega = \frac{2\pi \int_0^{r_o} UWr^2 \, \mathrm{d}r}{\pi r_o^3 U_m^2} \tag{15}$$

of the present case is 0.97, where U, W and U_m are the axial, tangential and bulk velocity respectively, r and r_o are the radial position and pipe radius. This swirl intensity corresponds to a swirl number of 0.85. Due to the presence of the high swirl intensity at the inlet and the absence of the central jet as observed in the previous case, extensive reverse flow is present in most of the flow domain. Experimental data are available from $X/d_o = 5.7$ pipe diameter downstream of the test section at which point the numerical simulation starts. It should be pointed out that the inlet plane straddles across the recirculation zone.

The most dramatic effect of the model's performance can be referred to the centreline axial velocity distributions, shown in Figure 7, and the axial and tangential velocity profiles, shown in Figures 8 and 9. It can be clearly seen that both the k–ϵ and IPCM models predict overexcessively diffusive profiles. In strong contrast, both the measurements and SSG model indicate an extended region of recirculation zone. The excessive nature of k–ϵ model in strongly swirling flow is consistent to what was observed previously. However, the IPCM model's performance needs to be further investigated.

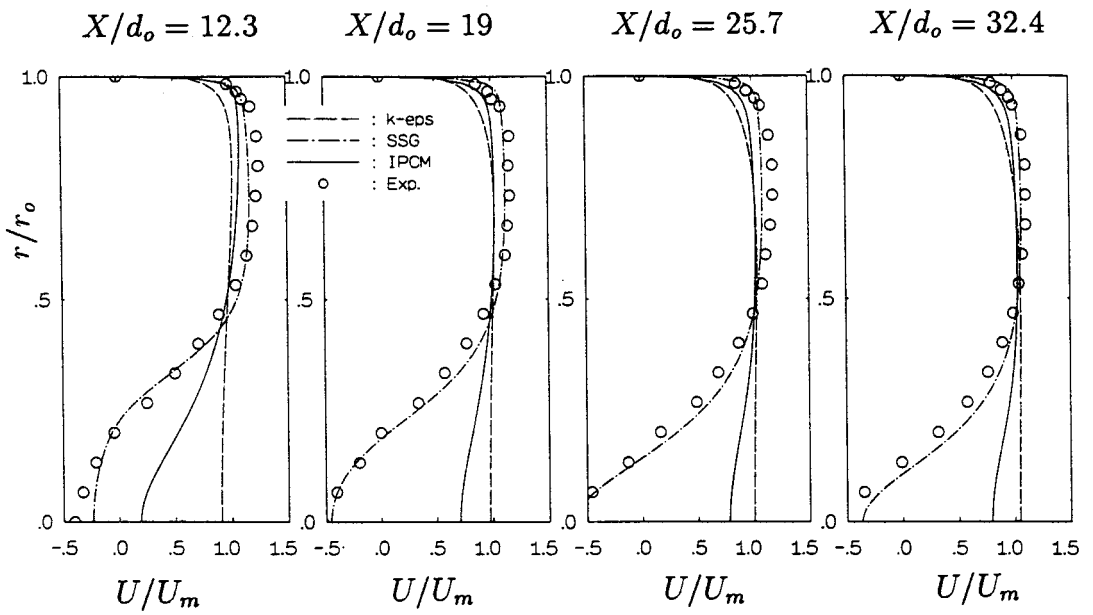

Figure 8. Axial velocity distributions—Kitoh's case.

The cause of this behaviour can be traced back to the formulation of the modelled form of pressure–strain process. The pressure–strain term of $\overline{uv}$ of the SSG model can be expressed in terms of that of IPCM and is as,

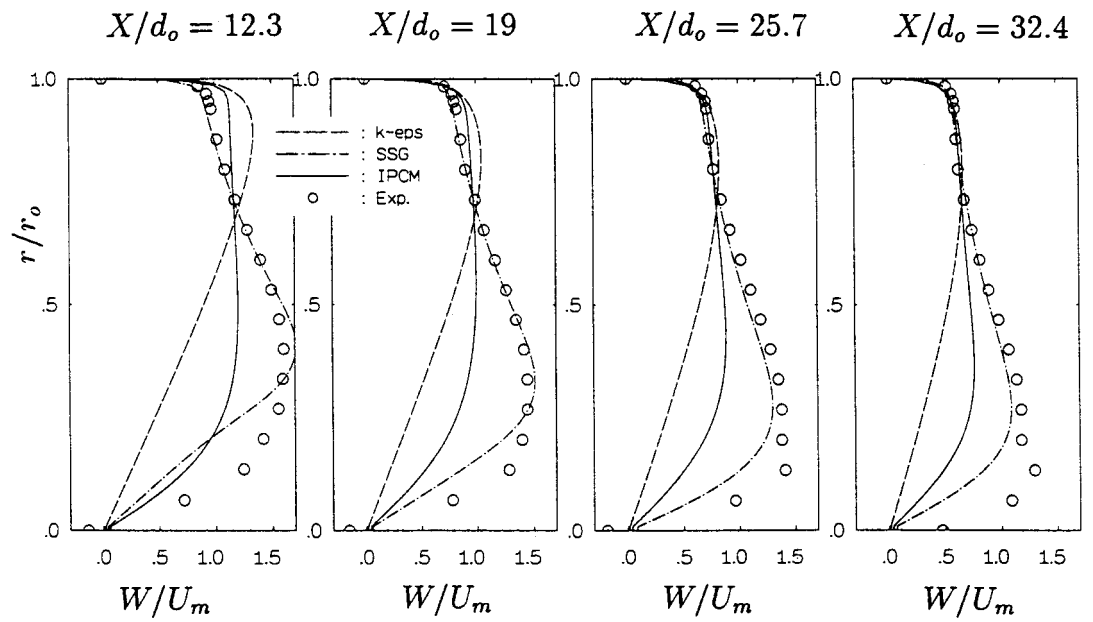

Figure 9. Tangential velocity distributions—Kitoh's case.

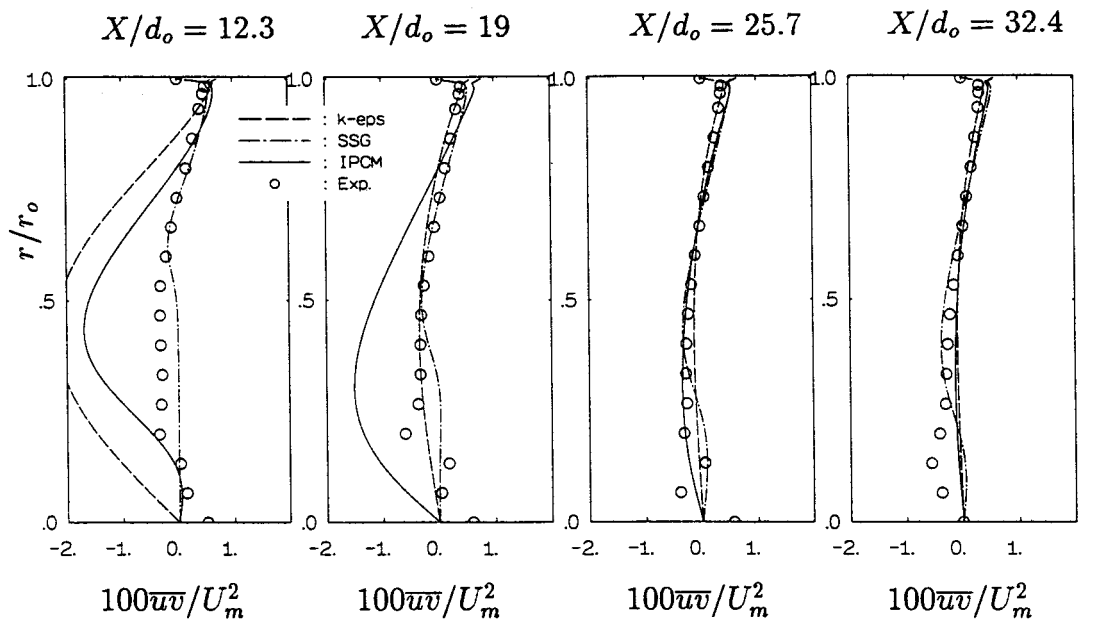

Figure 10. $\overline{uv}$ distributions—Kitoh's case.

$$(\phi_{\overline{uv}})_{\mathrm{SSG}} = (\phi_{\overline{uv}})_{\mathrm{IPCM}} + \underbrace{\epsilon\left(0.2 - 1.8\frac{P_k}{\epsilon}\right)b_{12}}_{A} + \underbrace{4.2\epsilon[(b_{11}+b_{22})b_{12} + b_{13}b_{23}]}_{B}$$
$$\underbrace{-0.65\sqrt{b_{kl}b_{kl}}\,k\frac{\partial U}{\partial r}}_{C} + \underbrace{k(0.425b_{11} - 0.375b_{22})\frac{\partial U}{\partial r}}_{D}$$
$$\underbrace{+ kb_{13}\left(0.425\frac{\partial W}{\partial r} + 1.575\frac{W}{r}\right)}_{E}, \tag{16}$$

where the wall reflection terms of IPCM have been neglected. It should be noted that terms B, C and the production related part of term A do not exist in the linear pressure strain models.

The reduced level of the shear stress predicted by the SSG model, shown in Figure 10 at $X/d_o = 12.3$ can be traced back to the formulations of the pressure–strain process. It is clear that the major terms A, D act as extra sink terms, relative to IPCM model, for predicted $\overline{uv}$ adopting SSG model. Across the non-equilibrium shear layer where the production term P_k is much higher than the turbulence dissipation rate ϵ, this makes the effect of term A even more pronounced. This reduced level of shear stresses, predicted by SSG and shown in Figures 10–12, is consistent with what was observed earlier of the mean velocity profiles.

Figures 13–15 show the predicted normal stresses. It is not surprising to observe that SSG predicts a lower level of $\overline{v^2}$ at $X/d_o = 12.3$ and 19. This is consistent with what was observed in the distributions of $\overline{uv}$ predicted by the SSG model. As was observed in the $\overline{uv}$ equation, the production related term in the SSG model seems to have profound effect on the stresses. By examining the pressure–strain term of the normal stresses, the SSG model gives

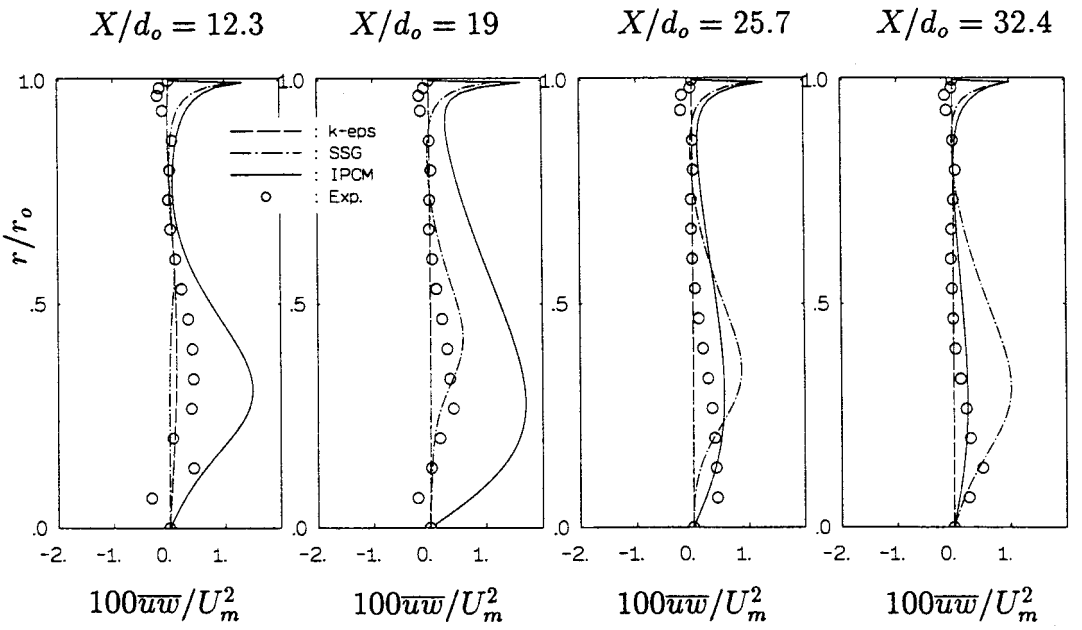

Figure 11. $\overline{uw}$ distributions—Kitoh's case.

$$(\phi_{\overline{uu}})_{\mathrm{SSG}} = (\phi_{\overline{uu}})_{\mathrm{IPCM}} + \epsilon\left(0.2 - 1.8\,\frac{P_k}{\epsilon}\right)b_{11} + \cdots \tag{17}$$

$$(\phi_{\overline{vv}})_{\mathrm{SSG}} = (\phi_{\overline{vv}})_{\mathrm{IPCM}} + \epsilon\left(0.2 - 1.8\,\frac{P_k}{\epsilon}\right)b_{22} + \cdots \tag{18}$$

$$(\phi_{\overline{ww}})_{\mathrm{SSG}} = (\phi_{\overline{ww}})_{\mathrm{IPCM}} + \epsilon\left(0.2 - 1.8\,\frac{P_k}{\epsilon}\right)b_{33} + \cdots \tag{19}$$

It can be observed that the production related term will be influential in regions where the ratio of P_k/ϵ is large. Therefore, a more isotropic stress field predicted by SSG is expected in regions across the shear layer where the strain rate is high.

5. CONCLUSION

Computations of strongly swirling flows were performed by k–ϵ model and variants of Reynolds stress transport model with linear (IPCM) and quadratic (SSG) form of the pressure–strain models. Comparisons of the predictions with measurements indicated that for the $S = 2.25$ case, due to the inherent capability of the Reynolds stress models to capture the strong swirl and turbulence interaction, both the linear and quadratic form of the pressure–strain models predict the flow adequately. In strong contrast, the k–ϵ model predicts an excessively diffusive flow fields. For the swirl number 0.85 case, both the k–ϵ and Reynolds stress model with linear pressure–strain process, show an excessively diffusive transport of the flow fields. The correct axial flow development predicted by SSG was attributed to the lower level of $\overline{uv}$ predicted by the models, and this could be traced back to the modelled form of the

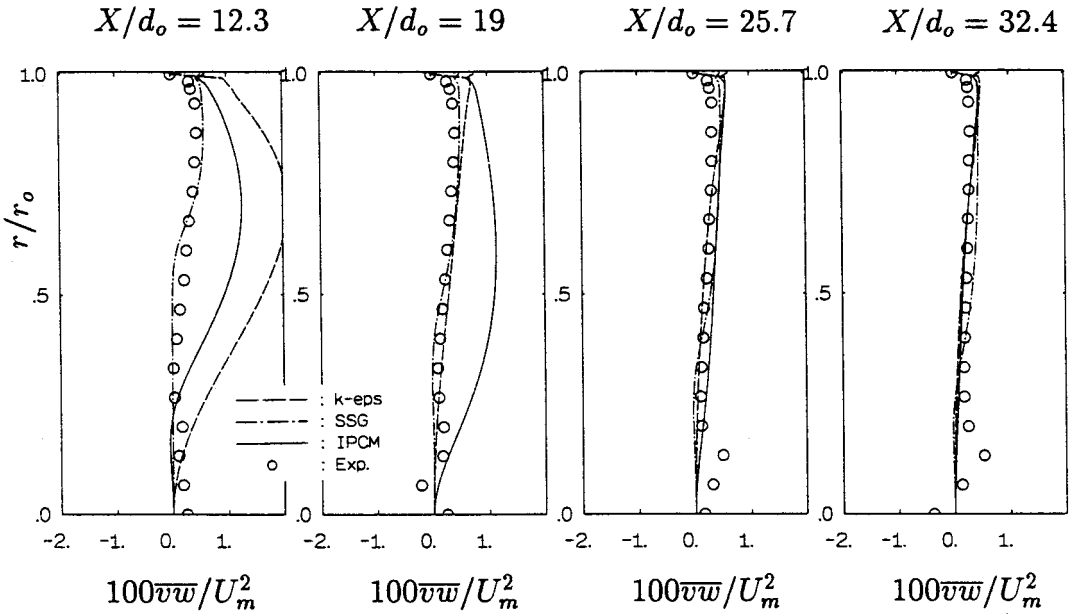

Figure 12. $\overline{vw}$ distributions—Kitoh's case.

pressure–strain term, after examining the formulations of the pressure–strain models. Overall, the SSG model is found to produce lower level of turbulence in regions of high shear and this agrees with what the measurements show.

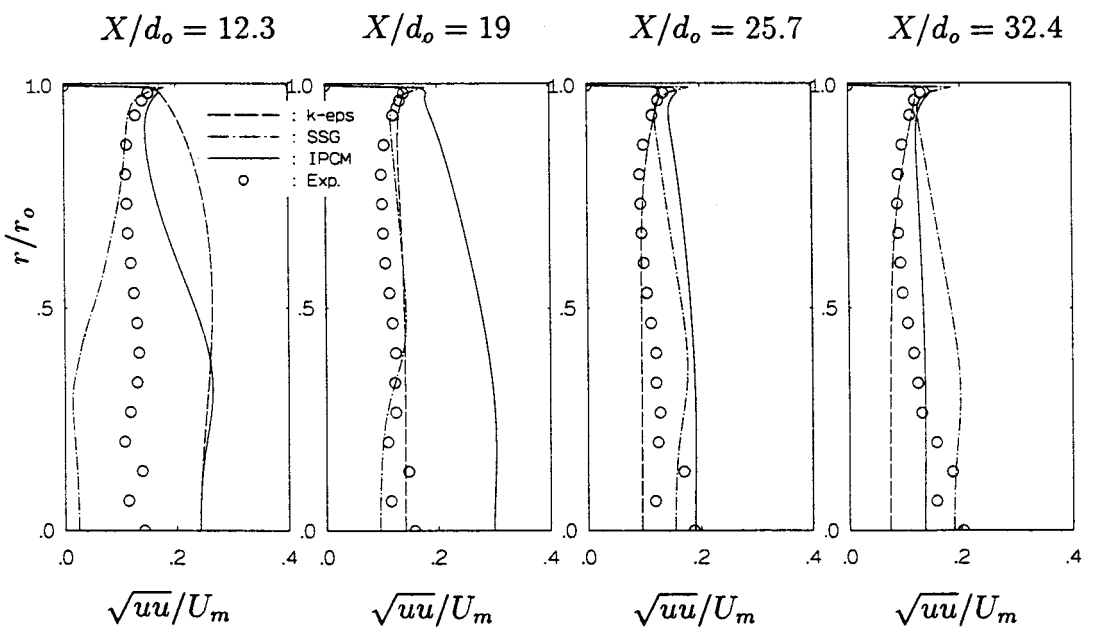

Figure 13. $\overline{uu}$ distributions—Kitoh's case.

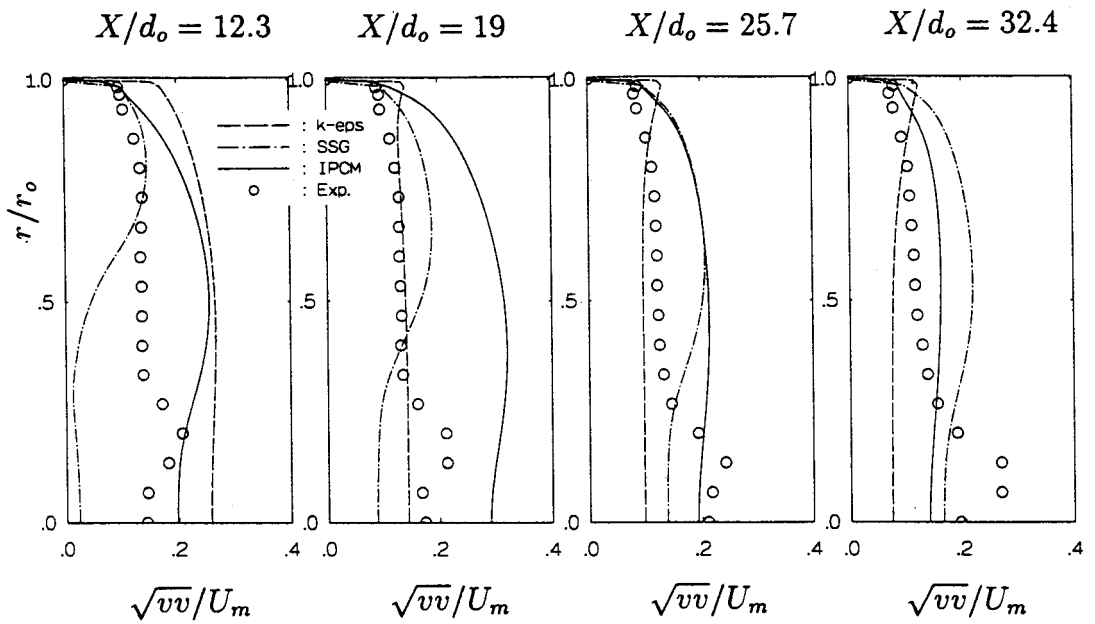

Figure 14. $\overline{vv}$ distributions—Kitoh's case.

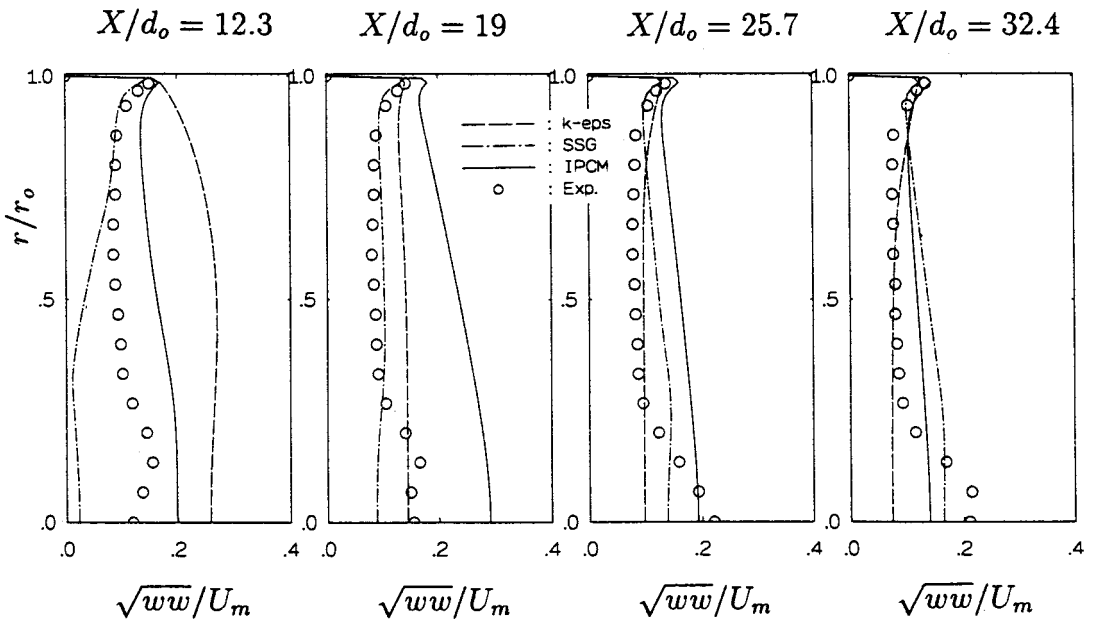

Figure 15. $\overline{ww}$ distributions—Kitoh's case.

ACKNOWLEDGMENTS

This research work was supported by the National Science Council of Taiwan under grant NSC85-2212-E-007-023 and the computational facilities were provided by the National Centre for High Performance Computing of Taiwan which the authors gratefully acknowledge.

APPENDIX A. NOMENCLATURE

b_{ij}	the Reynolds stress anisotropy tensor
$C_{\epsilon 1}$, $C_{\epsilon 2}$	turbulence model coefficient
C_{ij}	convection tensor of Reynolds stresses
d_{ij}	diffusion tensor of Reynolds stresses
d_j	jet diameter
d_o	pipe diameter
H	step height of sudden expansion
k	turbulent kinetic energy
L	turbulence length scale
n_i	unit vector
P_{ij}	production tensor of Reynolds stresses
r	radial distance
r_o	pipe radius
S	swirl number
U	axial velocity
U_{in}	inlet axial velocity
U_j	axial jet velocity
$\underline{U_m}$	axial bulk velocity
$\overline{u_i u_j}$	Reynolds stress tensor
V	radial velocity
X	axial direction distance
y^+	dimensionless distance in wall function
y_v	thickness of the viscous sublayer
W	tangential velocity

Greek letters

δ_{ij}	Kronecker delta
ϵ	turbulent dissipation rate
ϵ_{ij}	turbulent dissipation rate tensor
μ	viscosity
ϕ_{ij1}, ϕ_{ij2}, ϕ_{ijw}	pressure–strain tensor
ρ	mean density
σ	Prandtl number
ω	angular velocity
Ω	swirl intensity

Subscripts

i, j, k	tensorial direction indices
in	flow inlet
l	laminar
t	turbulent

REFERENCES

1. B.E. Launder, 'Second-moment closure—methodology and practice', in *Turbulence Models and their Applications*, Vol. 2, CEA-EDF INRIA Ecole d'ete d'analyse numerique, Eyrolles, 1984.

2. M.M. Gibson and B.A. Younis, 'Calculation of swirling jet with a Reynolds stress closure', *Phys. Fluids*, **29**, 38–48, 1435–1443 (1986).
3. S. Fu, B.E. Launder and M.A. Leschziner, 'Modelling strongly swirling recirculating jet with Reynolds stress transport closure', *Proc. 6th Symp. on Turbulent Shear Flows*, Toulouse, 1987, pp. 17.6.1–17.6.6.
4. S. Fu, P.G. Huang, B.E. Launder and M.A. Leschziner, 'A comparison of algebraic and differential second-moment closure for axisymmetric turbulent shear flows with and without swirl', *J. Fluids Eng. Trans. ASME*, **110**, 216–221 (1988).
5. S. Hogg and M.A. Leschziner, 'Computation of highly swirling confined flow with a Reynolds stress turbulence model', *AIAA J.*, **27**, 57–63 (1989).
6. D. Wennerberg and S. Obi, 'Predictions of strongly swirling flows in quarl expansions with a non-orthogonal finite volume method and a second-moment turbulence closure', *Proc. 2nd Int. Symp. on Engineering Turbulence Modelling and Measurements*, Florence, Italy, 31st May–2nd June, 1993, pp. 197–206.
7. C.H. Lin, C.A. Lin and J.C. Chen, 'Modelling influences of inlet swirl profiles on dump combustor flows', *AIAA J.*, **34**, 2630–2632 (1996).
8. R.M.C. So, S.A. Ahmed and H.C. Mongia, 'An experimental investigation of gas jets in confined swirling air flow', *NASA CR3832*, 1984.
9. O. Kitoh, 'Experimental study of turbulent swirling flow in a straight pipe', *J. Fluid Mech.*, **225**, 445–479 (1991).
10. W.P. Jones and B.E. Launder, 'The prediction of laminarisation with a two-equation model of turbulence', *Int. J. Heat Mass Transf.*, **15**, 301–314 (1972).
11. C.G. Speziale, S. Sarkar and T.B. Gatski, 'Modelling the pressure–strain correlation of turbulence: an invariant dynamical approach', *J. Fluid Mech.*, **227**, 245–272 (1991).
12. C.A. Lin and M.A. Leschziner, 'Three-dimensional computation of transient interaction between radially injected jet and swirling cross-flow using second-moment closure', *Comput. Fluid Dyn. J.*, **1**, 423–432 (1993).
13. S.V. Patankar, *Numerical Heat Transfer and Fluid Flow*, Hemisphere Publishing, New York, 1980.
14. B.P. Leonard, 'A stable and accurate convective modelling procedure based on quadratic upstream interpolation', *Comp. Methods Appl. Mech. Eng.*, **19**, 59–98 (1979).
15. S.A. Ahmed and A.S. Nejad, 'Swirl effects on confined flows in axisymmetric geometries', *J. Propul. Power*, **8**, 339–345 (1992).
16. H.B. Squire, 'Analysis of the vortex breakdown phenomenon', *Miszellanen der Angewandten Mechanik*, Akademic, Berlin, 1962, pp. 306–312.
17. M.P. Escudier and J. Keller, 'Recirculation in swirling flow: a manifestation of vortex breakdown', *AIAA J.*, **23**, 111–116 (1985).

